ACS APPLIED NANO MATERIALS
Cite This: ACS Appl. Nano Mater. 2019, 2, 8063−8074
Article
www.acsanm.org

Fe/N-Codoped Hollow Carbonaceous Nanospheres Anchored on Reduced Graphene Oxide for Microwave Absorption

Kaifeng Wang, Yujie Chen, Hua Li,* Bingbing Chen, Kun Zeng, Yongle Chen, Haochang Chen, Qinglei Liu, and Hezhou Liu

State Key Laboratory of Metal Matrix Composites, School of Materials Science and Engineering, Shanghai Jiao Tong University, Shanghai 200240, People's Republic of China

Supporting Information

ABSTRACT: To alleviate and even eliminate electromagnetic pollution problems, it is inevitable to evolve materials that exhibit a desirable effect on attenuating microwaves with broad response frequency bandwidth and high absorption capacity, while thickness and weight are equally important. The combination of Fe/N-codoped carbon-based nanospheres (0 dimension) and graphene (2 dimension) are highly desirable for improving microwave absorption properties due to producing advantages between different portions. Herein, hollow Fe_3O_4 nanoparticles were selected as a hard template; through oxidation polymerization and high temperature carbonization processes in inert atmosphere, the designed structure, Fe/N-codoped hollow carbonaceous nanospheres, was anchored on the surface of reduced graphene oxide. As expected, the lightweight designed nanocomposites exhibited enhanced microwave absorption properties due to increased polarization loss (interfacial and dipole polarization), conductivity loss, and multiple resonance behaviors, with the minimum value of reflection loss achieved as −49.08 dB at 7.15 GHz, while the thickness is 2.5 mm, and the filler ratio is only 5%. In addition, the effective absorption bandwidth can be tuned from 3.1 to 18 GHz, validating them as promising next-generation microwave absorbing materials during practical application.

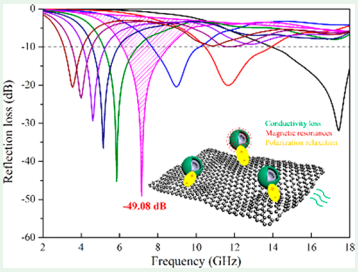

KEYWORDS: *microwave absorption, interfacial polarization, graphene, hollow shell, dielectric loss, magnetic loss*

1. INTRODUCTION

With the prosperity of science and technology, high-tech communication facilities are required in both civil and military fields, which require urgent resolution of the problems caused by current electromagnetic wave (EMW) pollution.[1−4] Consequently, EMW-absorbing materials with high absorbing capability are in high demand. With respect to the energy dissipation mechanism, conventional EMW absorbers can be broadly divided into dielectric-loss materials and magnetic-loss materials that have different mechanisms of microwave absorption.[5−8] Many efforts have been undertaken to obtain high-performance EMW absorbers, especially in the gigahertz (GHz) range. Magnetic absorbers,[9−11] which include ferromagnetic (Fe, Ni, Co), ferrite, and related magnetic composites, can significantly weaken the EM waves by natural ferromagnetic resonance, exchange resonance, and eddy current effect in the frequency range of 2−18 GHz. However, the magnetic metal nanoparticles (those that possess a high value of saturation magnetization with Snoek's limit[12,13] in the gigahertz frequency ranges), which can produce an enormous magnetic loss, experience restricted usage owing to their poor corrosion resistance and high density. However, dielectric absorbers, which include carbon-based materials,[14−18] conjugated polymers,[19−22] and ceramic materials,[23,24] can absorb electromagnetic energy due to their high electrical conductivity and powerful polarization-relaxation process. Carbon-based materials, especially the low-dimensional materials,[25,26] have been widely used as microwave absorbers since they possess significant dielectric-loss ability with good corrosion resistance, good electrical conductivity, large specific surface area, and ultralight weight. Moreover, doping N atoms into the carbon framework can introduce active cavities into the structure,[27−29] enabling the generation of uneven charge distribution, which is beneficial for producing polarization, thereby enhancing the dielectric-loss ability of the microwave absorbers.

Because single-loss-factor microwave-absorbing materials cannot simultaneously provide adequate magnetic loss and high dielectric loss, double-loss mechanisms and the synergistic effect between dielectric and magnetic constituents are required to satisfy the strict requirements of excellent microwave-absorption performance. Consequently, combinations of ferromagnetic and carbon-based materials were adopted by many researchers,[30−33] which possess the advantages of easy-accessibility, compatibility, and low cost. Among the various kinds of construction of microwave-absorbing composites, a core−shell structure[34−38] exhibits distinct positive advantages including enhanced interfacial polarization, facile synthesis methods, multiabsorption behaviors, and corrosion resistance of the inner core: these advantages assist in transforming, attenuating, and dissipating microwaves by effectively and

Received: November 7, 2019
Accepted: December 5, 2019
Published: December 5, 2019

DOI: 10.1021/acsanm.9b02192
ACS Appl. Nano Mater. 2019, 2, 8063−8074

efficiently converting electromagnetic energy to thermal energy. Chen et al.[37] synthesized porous Fe_3O_4/C nanorods with a core−shell structure using the hydrothermal method and annealing treatment; a minimum reflection loss value of −27.9 dB was obtained at 14.96 GHz for a thickness of 2 mm, suggesting the suitability of using these specific composites in the microwave absorption region. Our group[39] synthesized a Co@C core−shell structure via the facile post-treatment of Co-MOF-74 and obtained a superior microwave reflection loss value of −62.12 dB. However, the solid metallic cores used were heavy, violating the prerequisite lightweight requirement of next-generation microwave absorbers. Herein, hollow structures[40,41] have captured attention for their prominent contribution to reduce weight, and they have been used in fields such as biomedical science, catalysis, batteries, and giant magnetoresistance induction. Moreover, the increase in interfacial specific surface areas[42] also shows potential in microwave absorption, which can be achieved by combining 0-dimensional nanoparticles and 2-dimensional nanosheets. Therefore, the design of hollow-core/shell nanoparticles anchored on nanosheets, exhibiting both dielectric loss and magnetic loss mechanisms, has become an irreplaceable and promising trend to replace the conventional structures in the future.

In this study, hollow iron oxide (H-Fe_3O_4) nanoparticles are employed as the hard template. Further, when combined with graphene oxide, Fe/N-codoped hollow carbonaceous nanospheres anchored on reduced graphene oxide (Fe/N-C−RGO) are synthesized via the hydrothermal method with self-template-oxidized polymerization, followed by high-temperature calcination in an inert atmosphere. The synergistic effect between zero-dimensional hollow nanospheres and two-dimensional reduced graphene oxide significantly influences the properties of the absorbers. The minimum value of the reflection loss attains a value of −49.08 dB at a frequency of 7.15 GHz with a thickness of 2.5 mm, while the absorbers constitute only 5% of the filler. In addition, it shows a bandwidth of reflection loss smaller than −10 dB for the response frequency ranging from 3.1 to 18 GHz, covering 93.13% of the whole microwave frequency range. In this material, the absorber primarily comprises carbon-based materials, which are significantly more lightweight than most reported materials. Compared with those of a hollow iron oxide precursor, it exhibits a promising enhancement in the microwave absorption properties; further, it provides an effective and successful synthesis as well as enhances the development of composites in practical applications.

2. EXPERIMENTAL SECTION

2.1. Fabrication of Porous Hollow Fe_3O_4 Template. The hollow Fe_3O_4 nanospheres were prepared via hydrothermal reaction. Typically, $FeCl_3{\cdot}6H_2O$ (0.005 mol) was dissolved in ethylene glycol (70 mL) with sonication, followed by the addition of ammonium acetate (0.05 mol) mixed into the former transparent yellow solution with continuous sonication for an hour. After that, the homogeneous vicious solution was transferred into a Teflon-lined stainless-steel autoclave and heated in the chamber of a blast oven at 200 °C for 8 h. The obtained black precipitates were separated from the solvent and washed with ethanol through centrifugation three times after cooling down to room temperature naturally, followed by drying in vacuum at 60 °C for the whole night.

2.2. Fabrication of Intermediate Fe-Based/Polypyrrole Nanospheres Anchored on Graphene Oxide. The Fe-based/polypyrrole nanospheres anchored on graphene oxide (Fe/PPY−GO) were prepared through an in situ polymerization process. To be specific, hollow Fe_3O_4 nanospheres (0.15 g) were dispersed on graphene oxide (GO) after ultrasonication for 1 h, followed by dropping pyrrole monomers (2 mL) with continuous sonication to make sure that the pyrrole monomers fully covered the outer and inner surface of hollow Fe_3O_4 nanospheres. After that, hydrochloric acid (6%, 1 mol/L) was mixed into the reaction, and the mixture was kept under sonication. Some sediment appeared gradually, which means pyrrole monomers were carrying on in situ oxidized polymerization on the interfaces of Fe_3O_4 nanospheres. After full reaction, the black product was centrifuged with ethanol three times and dried at 60 °C in a vacuum oven for 12 h. By comparison, hollow Fe_3O_4 anchored on reduced graphene oxide was fabricated by a hydrothermal method, which is similar to the fabrication of the hollow Fe_3O_4, except adding quantities of GO named as H-Fe_3O_4−RGO into aqueous solution with stirring. In addition, though controlling the polymerization time, nanocomposites with different Fe contents were obtained similarly.

2.3. Fabrication of Fe/N-Codoped Hollow Carbon Nanospheres Anchored on Reduced Graphene Oxide. In order to transform conductive PPy into Fe/N-codoped carbon-based shells, Fe/PPY−GO was placed in corundum crucibles and pyrolyzed in a quartz tube at 750 °C for an hour, with a given ramp rate (5 °C/min) in an atmosphere of high purity argon. After the calcination process, Fe/N-codoped hollow carbon nanospheres anchored on reduced graphene oxide (Fe/N-C−RGO) were obtained.

2.4. Characterization. The crystalline structure of the composite was measured by powder X-ray diffraction (pXRD, Rigaku) on a D/max X-ray diffractometer with Cu Kα radiation (λ = 0.15418 nm) at a scan speed of 5°/min. The thermal properties of Fe/PPY−GO were analyzed through thermal gravimetric analysis (TGA) measurements on SDT-Q600 at a heating rate of 10 °C/min from 20 to 800 °C in an inert atmosphere (N_2). The chemical compositions of the elements were detected through X-ray photoelectron spectroscopy (XPS) on an Axis Ultra DLD spectrometer (Kratos). A magnetic property measurement system (MPMS3, Quantum Design) was used to measure magnetic properties of the samples at room temperature with the magnetization field from −30000 to 30000 Oe. An accelerated surface area and porosimetry system (ASAP2460, Micromeritics Instrument Corporation) was used to obtain the surface areas and the pore size distribution of the samples. The electrical conductivity was tested using a four-point probe resistivity measurement system. FT-IR spectroscopy was carried out on a Nicolet 6700 FT-IR spectrometric analyzer with KBr pellets. Atomic force microscopy (AFM) was adopted to evaluate the number of layers of reduced graphene oxide. The intensity of Raman spectra (with wavenumber ranges from 45 to 4000 cm^{-1}) and scanning electron microscopy (SEM) images were obtained together on a scanning electron microscope−Raman spectroscopy combined system (RISE-MAIA 3 GMU SEM), while the spot size of Raman spectra was 2 mm on a 532 nm argon ion laser (10 mW), and the acceleration voltage was 5 kV. After the samples were pretreated by embedding in epoxy resin in a lacey support film and ultrathin sectioning, the atomic structure of the interfaces, transmission electron microscopy (TEM) with high-angle annular dark field (HAADF) images, elemental mapping spectra, and selected area electric diffraction (SAED) were performed by utilizing a high resolution TEM system (JEM-ARM200F) equipped with cold field emission gun and Cs correctors (CEOS GmbH, Heidelberg, Germany), in order to demonstrate the morphology of the nanocomposites, the distribution of different elements, and the degree of crystallinity of the graphitic carbon in depth.

For electromagnetic parameter (the real and imaginary parts of permittivity and permeability) measurement, the Fe/N-C−RGO samples were dispersed in paraffin wax (which is transparent to electromagnetic waves) homogeneously with a mass ratio of only 5%, followed with pressing them into 3 mm-thick rings with inner diameter of 3.04 mm and outer diameter of 7 mm. After the pretreatment, those parameters were measured at frequency range from 2 to 18 GHz through a vector network analyzer (VNA, Agilent N5224A) with the guidance of transmission/reflection coaxial line method.

DOI: 10.1021/acsanm.9b02192
ACS Appl. Nano Mater. 2019, 2, 8063−8074

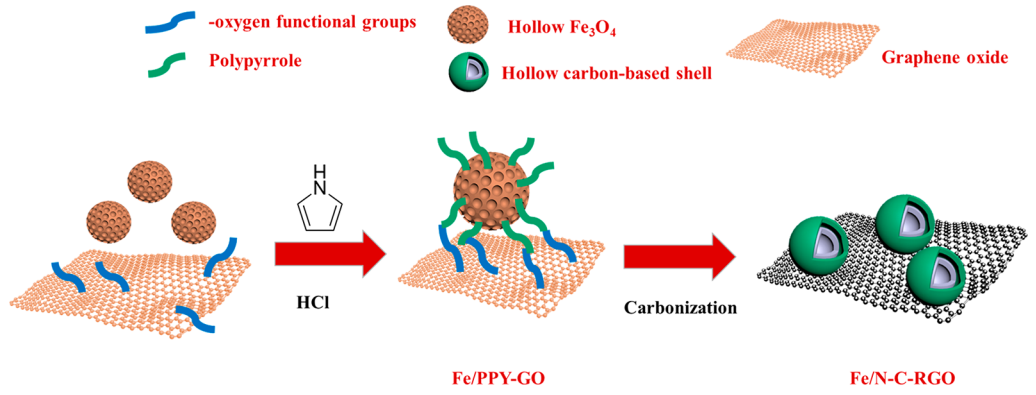

Figure 1. Schematic representation of the fabrication of the Fe/N-C−RGO microwave absorber.

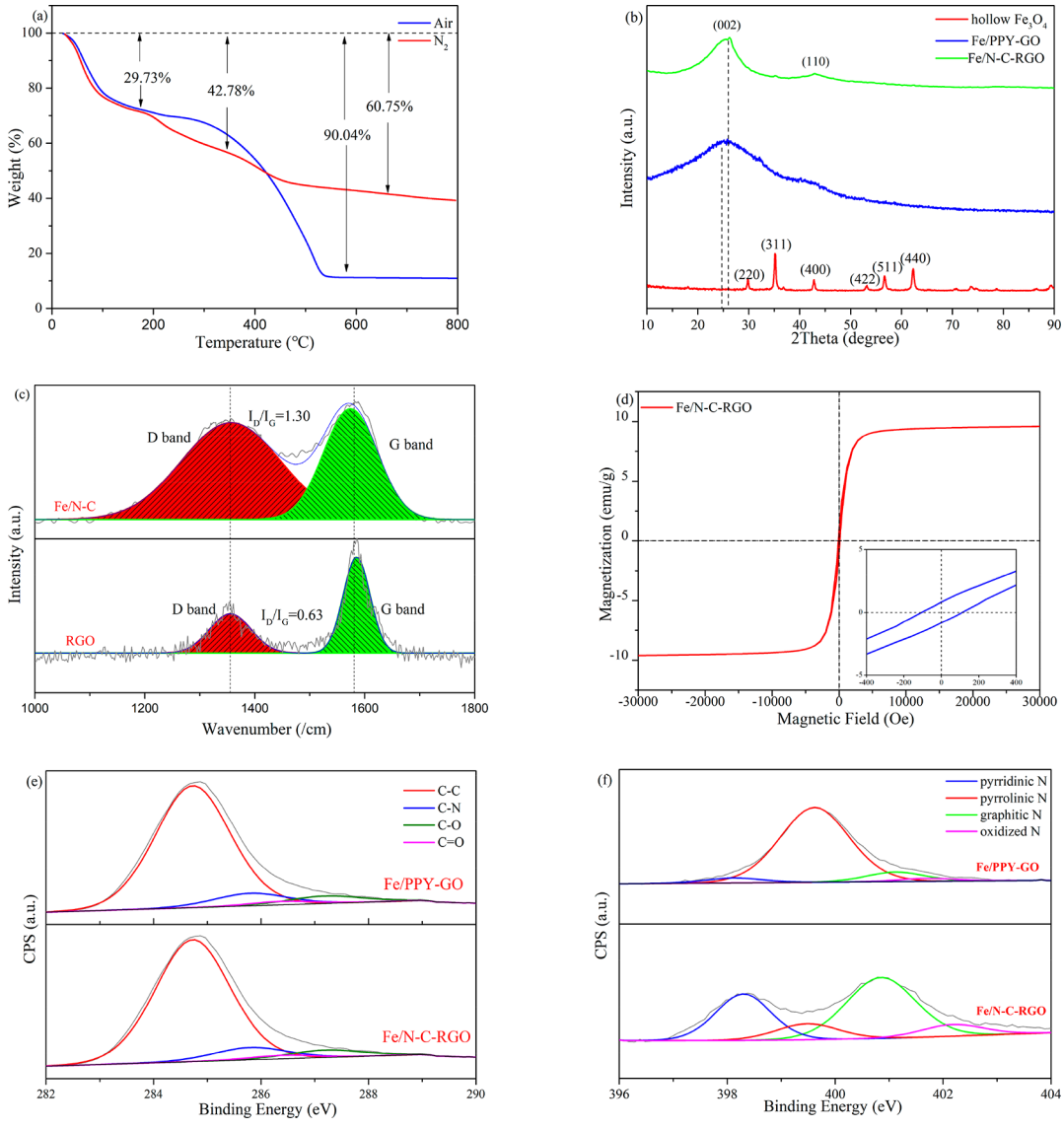

Figure 2. (a) TG curves of Fe/PPY−GO; (b) XRD patterns, (c) Raman spectra, (d) PPMS curves, and C 1s (e) and N 1s (f) XPS spectra of Fe/N-C−RGO and correspondences.

3. RESULTS AND DISCUSSION

The preparation process of Fe/N-C−RGO nanocomposites is schematically shown in Figure 1. The hollow-structured Fe_3O_4 nanoparticles were initially prepared through the hydrothermal method. Ferric chloride ($FeCl_3 \cdot 6H_2O$) was employed as the Fe resource, whereas ethylene glycol was selected as the solvent because its hydroxyl functional groups can promote the reduction of Fe^{3+}. Meanwhile, this solvent possesses high viscosity and permittivity, which helps to dissolve the highly polar inorganic materials. Traditional sodium acetate

DOI: 10.1021/acsanm.9b02192
ACS Appl. Nano Mater. 2019, 2, 8063−8074

(CH_3COONa) was replaced by ammonium acetate (CH_3COONH_4) for dissolving the particles in order to prevent agglomeration and create a hollow core by releasing NH_3 inside the cavities during the hydrothermal reaction. Subsequently, Fe^{3+} ions were released from hollow Fe_3O_4 via acid etching, anchoring onto the surfaces of GO due to the electrostatic force between Fe^{3+} ions and numerous oxygen-containing functional groups. When the pyrrole monomers contact Fe^{3+} ions on the surface of nanoparticles, *in situ* oxidation polymerization occurs under an acidic environment. Through tuning the polymerization time, the content of dopant can be also controlled with different properties. Therefore, unique hollow-core Fe/PPY nanospheres were obtained and anchored on GO nanosheets. Notably, the nanospheres and nanosheets exhibit chemical bonding with each other, as they can be separated neither by physical ultrasonication nor by harsh high-temperature calcination. Eventually, the Fe/PPY−GO were set into a tube furnace surrounded by argon gas atmosphere. Calcination in inert atmosphere can decompose and transform the PPy coating into a N-doped carbon-based framework to be used as shells, while the residual Fe atoms were doped on the carbon shell, along with the reduction of GO into reduced GO (RGO). Finally, the Fe/N-codoped hollow carbonaceous nanospheres anchored onto reduced graphene oxide (Fe/N-C−RGO) were successfully fabricated, exhibiting the designed structure with ultralight weight.

The thermal gravimetric properties of Fe/PPY−GO were obtained under nitrogen atmosphere (Figure 2a). The initial weight loss of approximate 29.73% before 200 °C can be attributed to the evaporation of solvent molecules and residual water. With increasing temperature, the Fe/PPY−GO slowly loses weight by 13.05% until 600 °C, attributable to the decomposition of the unpolymerized molecule, implying that chemical interaction of polypyrrole does not occur yet. Upon increasing the temperature further, a sharp weight loss of 17.97% appears, representing the thermal decomposition of polypyrrole and the complete reduction of residual Fe_3O_4 to Fe. At this point, PPy is decomposed and transferred into the carbon shell with random doping of both Fe and N atoms, leading to the formation of Fe/N-codoped carbon-based nanospheres. Simultaneously, Fe promotes the graphitization of the carbon shell and the reduction of GO under high temperature. However, excessively high temperature will not only crystallize graphite but also contribute to a misbalance between dielectric loss and magnetic loss factors, leading to microwave reflection rather than absorption. Therefore, 750 °C was selected as optimal carbonization temperature in this situation. In addition, TGA measurement conducted under oxygen atmosphere illustrates that the Fe content of the composites is 6.95%; this amount of Fe ions can also serve as a ferromagnetic source. The crystalline structures of the nanoparticles were detected by the powder XRD pattern, shown in Figure 2b. First and foremost, the featured diffraction peaks of precursor (hollow Fe_3O_4) were detected, and the peaks showing at around 31.25° (d = 2.86), 36.82° (d = 2.44), 44.76° (d = 2.02), 55.62° (d = 1.65), 59.30° (d = 1.56), and 65.19° (d = 1.43) correspond well to the (220), (311), (400), (422), (511), and (440) planes of iron oxide ($Fd\bar{3}m$, JCPDS No. 26-1136), respectively, demonstrating a face-centered cubic (fcc) structure,[43] verifying the successful formation of Fe_3O_4 from a hydrothermal method, even through the hollow cores were induced. After the oxidation polymerization treatment of Fe^{3+}(derived from the release of Fe_3O_4 through acid etching), polypyrrole covers the surface of precursors, which can be verified by the broad swelling at around 24.7°, originating from the poor crystallinity of the PPy phase.[44] After undergoing the high-temperature reduction process, the PPy layer is transformed into the Fe/N-codoped carbon shell, while GO is reduced into RGO, determined by the (002) (d = 0.34 nm) plane at ∼26°. Since most of the Fe_3O_4 nanospheres were washed by HCl to release Fe^{3+}, the residual of Fe species served as dopant with only a weak swelling near 43° to be detected by the X-ray diffractometer, perhaps due to the (110) plane of α-Fe. The graphitization degree and bonding state of carbon atoms are closely related to the dielectric loss of carbon-based materials. However, these properties are different between Fe/N-codoped nanospheres and RGO nanosheets. To evaluate this character with selected area, a SEM−Raman combined system was chosen to replace the traditional Raman spectrometry (Figure 2c). As mentioned previously,[17] two distinct peaks at about 1350 and 1580 cm^{-1} were detected, which belonged to D band and G band, respectively. While the D band reflects the disorder degree, or the amount of defects, in the lattices of carbon atoms, G band reflects the stretching vibrations in sp^2 bonding or the graphitic degree. The integrated intensity ratio, calculated by I_D/I_G, is a parameter introduced to demonstrate the graphitization degree of carbon-based materials. This ratio for Fe/N-codoped carbonaceous nanospheres is 1.30, much higher than that of reduced graphene oxide nanosheets (0.63) and H-Fe_3O_4−RGO (1.09, synthesized via the one-step hydrothermal method; Figure S1). This result indicates that increased defects and disorder emerged due to the doping of Fe/N atoms into the shell of carbonaceous nanospheres, along with the suitable reduction (graphitization) degree of the RGO. These defects act as active sites or cavities on the carbon frameworks, inducing orientated currents from specific dimensions. Furthermore, the different intensity values between nanospheres and nanosheets cause the directional migration of energy under different dimensions, which can greatly improve dipole polarization and interfacial polarization,[45] enhancing the dielectric loss eventually. In addition to XRD and Raman spectrometry, AFM (Figure S2) was adopted to characterize the properties of RGO. The thickness of RGO was measured to be ∼4 nm. The magnetic-hysteresis (M-H) curves were characterized at room temperature, shown in Figure 2d, which can demonstrate the magnetic properties of Fe/N-C−RGO. In general, the "S" shape of the M-H curve in the figure represents the ferromagnetic characteristic of the samples. Specifically, the value of saturation magnetization (M_s) is 9.60 emu/g, which is clearly smaller than the value of the precursor (H-Fe_3O_4, 92.2 emu/g; Figure S3) owing to the introduction of the nonmagnetic carbon-based framework and the decomposition of Fe_3O_4, eventually reducing the magnetic response behaviors. In addition, the enlarged image of the central section of the M-H loop (inset of Figure 2d) displays the value of remnant magnetization (M_r) and coercivity (H_c) of Fe/N-C−RGO: its H_c value of 40 Oe is larger than that of hollow Fe_3O_4 (5 Oe), which is attributed to the reduction of ferromagnetism and the induction of doping, pores, and defects. However, this enhanced value of H_c makes a great contribution to the magnetic loss due to the occurrence of magnetic hysteresis behaviors.[46] When meeting with an electromagnetic wave, the nanocomposites will apply a reverse magnetic field to hinder the change of the outer magnetic field, followed by the transformation from EM energy to heat.[47] X-ray photoelectron spectroscopy (XPS) is an effective method to analyze the chemical compositions of specific elements. The general spectra

DOI: 10.1021/acsanm.9b02192
ACS Appl. Nano Mater. 2019, 2, 8063−8074

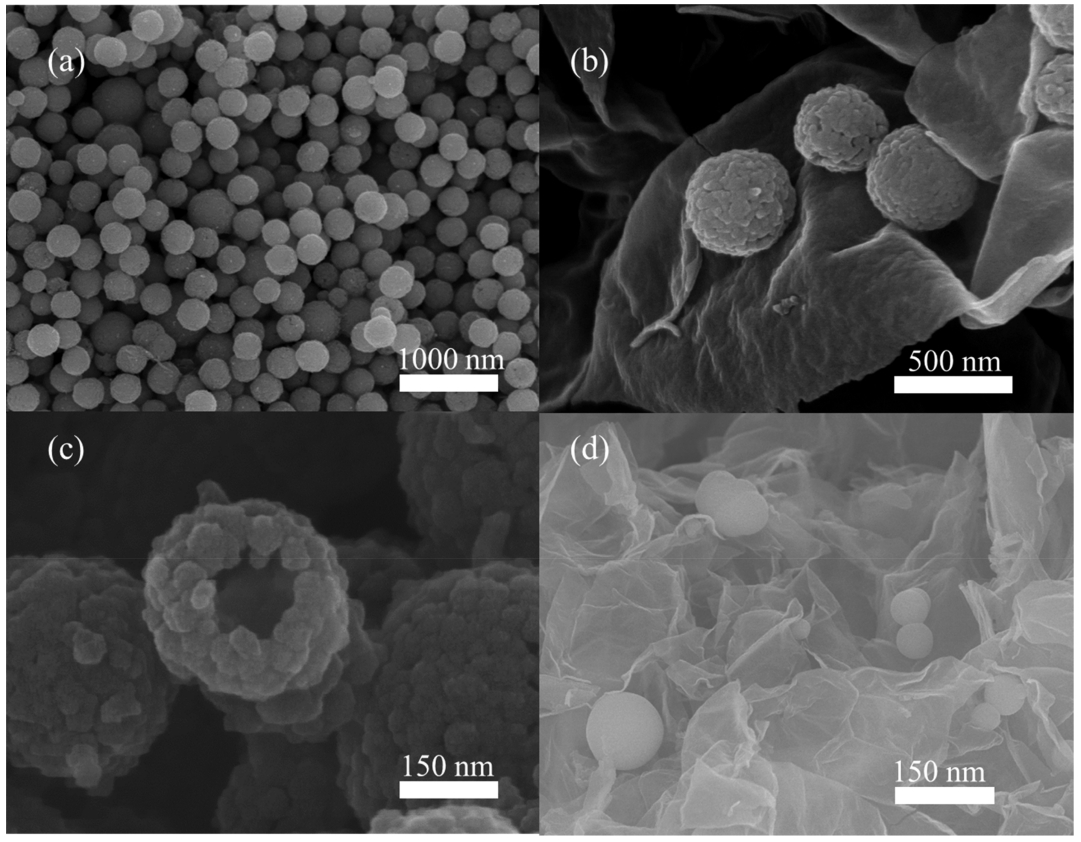

Figure 3. SEM images of (a) hollow Fe_3O_4, (b) Fe/PPY−GO, (c) fraction of Fe/PPY−GO, and (d) Fe/N-C−RGO.

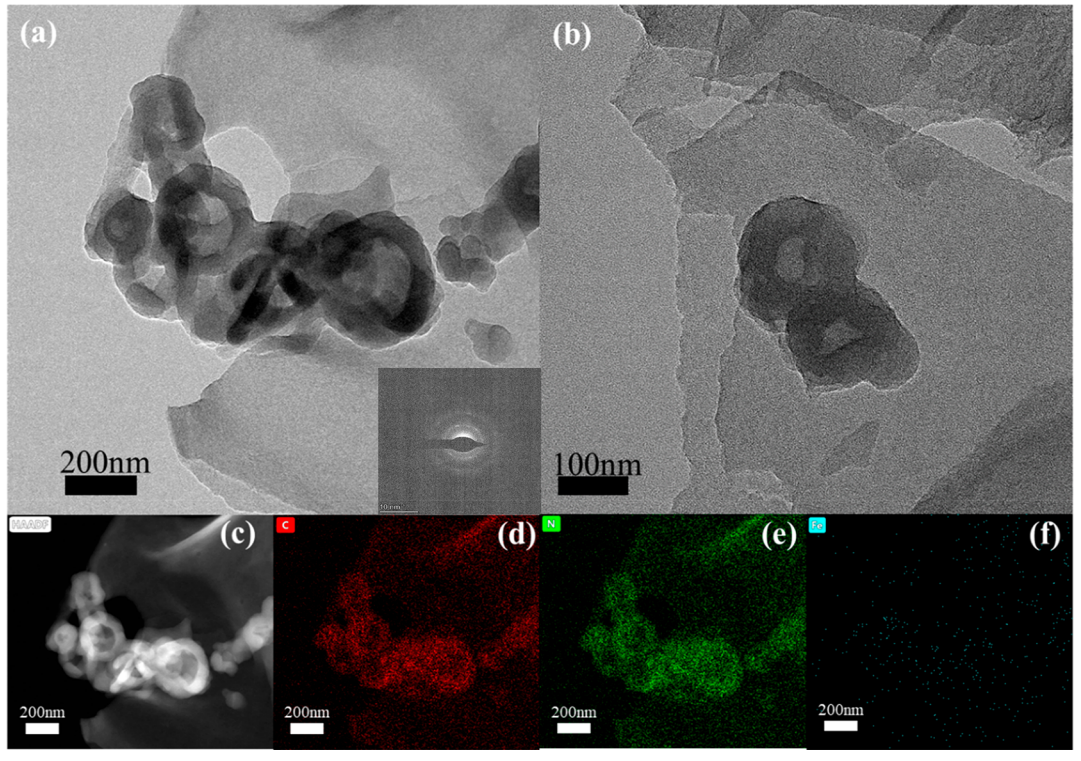

Figure 4. TEM images (a, b), corresponding HAADF (c), and EDX-mapping spectra of Fe/N-C−RGO, C (d), N (e), and Fe (f).

of Fe/N-C−RGO (Figure S4) predominantly exhibit the C 1s, N 1s, and O 1s peaks, while the signal of the Fe element is too weak to be detected. The O 1s peak is commonly attributed to the residual functional groups on the surface of RGO and the reflection of air on the interfaces. The high-resolution spectra of C 1s (Figure 2e) reveals four major peaks with binding energies

DOI: 10.1021/acsanm.9b02192
ACS Appl. Nano Mater. 2019, 2, 8063−8074

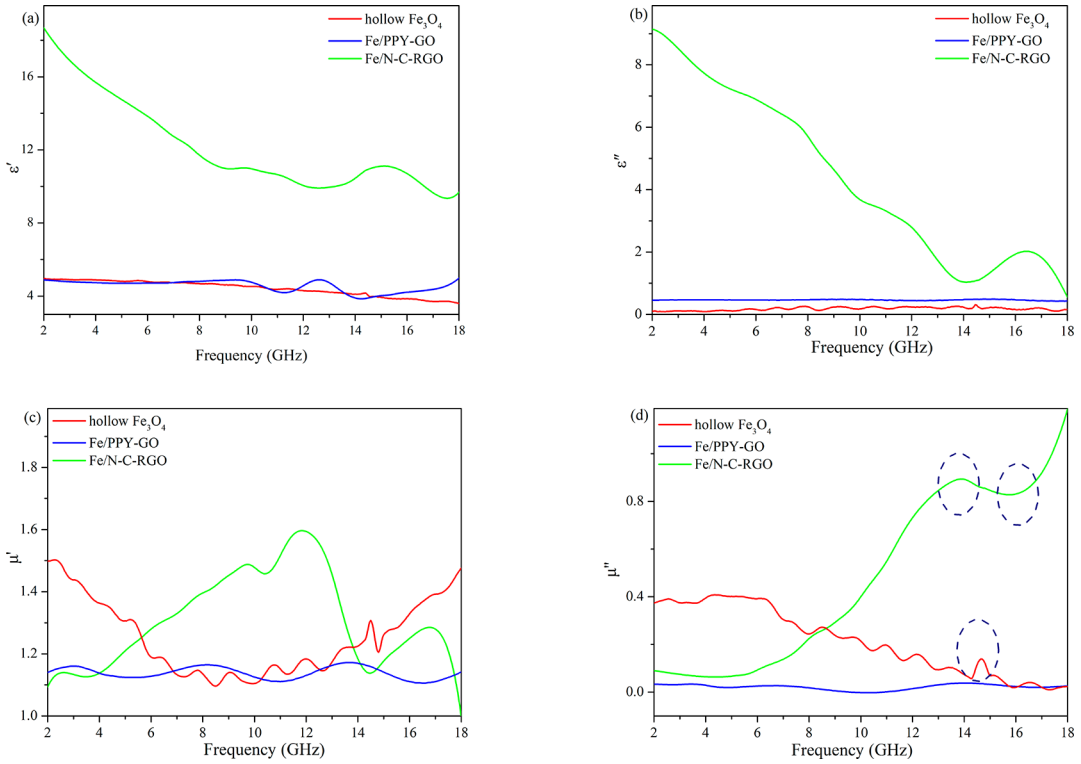

Figure 5. (a) Real and (b) imaginary parts of permittivity and (c) real and (d) imaginary parts of permeability of hollow Fe_3O_4, Fe/PPY−GO, and Fe/N-C−RGO.

of 284.7, 285.7, 286.3, and 287.1 eV, which are related to the C−C, C−N, C−O (epoxy/hydroxyl), and C═O (carbonyl) functional groups, respectively. The C−C sp^2 bonding at 284.7 eV can be attributed to the connection of the carbon-based framework in RGO and carbonaceous nanospheres. In addition, the C−N bonding is strong evidence for the occurrence of N atoms, which served as dopants, in the skeleton to construct a defective framework. C−O/C═O bonding seems to be the residual functional groups of RGO. The C 1s results are in agreement with the FT-IR results (Figure S5), which verify the chemical bonding in the sample. The N 1s spectrum, which is shown in Figure 2f, can be divided into four distinct nitrogen species, identified as pyridinic N (398.2 eV), pyrrolic N (399.5 eV), graphitic N (400.8 eV), and oxidized N (402.1 eV). These sources of N are generated from the decomposition of PPy. The existing forms of pyridinic N and graphitic N, which are the major components (a surplus of 86%) among nitrogen species, are believed to greatly contribute to microwave absorption, owing to offering more active sites for polarization centers, as well as enhancing the electrical conductivity (22.47 S/m compared to 1.18 S/m).[48] In addition, the porosity and specific surface area of Fe/N-C−RGO were detected using the Brunauer−Emmett−Teller (BET) system. According to the IUPAC classification the nitrogen adsorption−desorption isotherm shown in Figure S6 illustrates that I/IV-type curve existed, representing the occurrence of nanopores. The value of S_{BET} is calculated up to 309.03 m^2/g. The pore size distribution demonstrates an apparent peak at 3.42 nm.

The morphologies and microstructure of Fe/N-C−RGO were characterized with SEM (Figure 3). The representative image of the precursors (Figure 3a) shows evenly distributed nanospheres with a diameter of about 300 nm. At the initial stage, the pyrrole monomers, which filled the inner and dispersed in the outer space of the nanospheres, began to undergo the *in situ* oxidized polymerization process under catalysis from free Fe^{3+} ions (originating from the Fe_3O_4, released by HCl). Although Fe/PPY−GO inherits the spherical structure, the size of the nanospheres increased while the surface became rougher during the etching reaction, which can be observed from Figure 3b. A hollow core was found, which confirms that the core-in-hollow/shell structures were synthesized successfully. After a long period of catalysis, consecutive polypyrrole can be shaped into smooth shells that covered the interfaces between the Fe layer and air, while the hard-template would dissolve eventually. Notably, although covered with successive carbon coating, the particle size of Fe/N−C is slightly smaller than that of as-prepared Fe_3O_4 nanospheres after thermal decomposition treatment because of the shrinkage of nanospheres during the high-temperature calcination process (Figure 3d). More importantly, even after having experienced a harsh chemical reaction (high-temperature pyrolysis) and physical treatment (ultrasonication), the carbonaceous nanospheres were still embedded on the surface of RGO, which illustrates that strong chemical bonding, rather than physical incorporation, has contributed to connecting the different compositions.

TEM images (Figure 4) further elucidated the structure, morphology, and relative characterizations of Fe/N-C−RGO. The diameter of the hollow core is 140 nm for Fe/N−C nanospheres with a shell thickness of ∼40 nm. Clearly, the nanospheres (dark contrast) were evenly separated on the thin RGO surface (light contrast), constructing multidimensional nanocomposites. The inset images of Figure 4a show the SAED (selected area electron diffraction) pattern of the RGO nanosheets, which clearly reveal a weak graphitic crystalline structure of RGO along the [001] zone axis.[49] On the HR-TEM

DOI: 10.1021/acsanm.9b02192
ACS Appl. Nano Mater. 2019, 2, 8063−8074

image (Figure S7), multilayer graphitic carbon can be found on the edge of the nanospheres, but there was no crystalline Fe species, which verified that Fe is a dopant. High-angle annular dark field (HAADF) images were obtained using the STEM module, which clearly show the distribution of the following elements (Figure 4c): C, N, and Fe elements can be recognized by different contrast values in the HAADF image, wherein the larger the relative atomic mass, the brighter the element. The successful synthesis of the codoped nanostructure can also be verified via EDX-elemental mapping and energy element loss spectra (Figure 4d–f), exhibiting clearly distinguished compositions from different elements and confirming the structure. Notably, the Fe species were still homogeneously distributed in the nanocomposite to some extent, and they were mainly separated in the shell of the nanospheres, thereby inducing magnetic behavior in the samples. The results demonstrated the successful *in situ* formation of multidimensional nanocomposites, being of great potential in lightweight multifunctional carbon-based materials.

For representing the EMW-absorption properties, the reflection loss (RL) value is calculated by measuring complex permittivity and permeability with given frequency and thickness of the samples. The equations are shown as follows:[39]

$$\varepsilon_r = \varepsilon' - j\varepsilon'' \tag{1}$$

$$\mu_r = \mu' - j\mu'' \tag{2}$$

$$Z_{in} = Z_0\sqrt{\frac{\mu_r}{\varepsilon_r}}\tanh\left[j\left(\frac{2\pi}{c}fd\right)\sqrt{\mu_r\varepsilon_r}\right] \tag{3}$$

$$RL = 20\log\left|\frac{Z_{in} - Z_0}{Z_{in} + Z_0}\right| \tag{4}$$

Herein, ε_r and μ_r stand for the complex permittivity and permeability, respectively; Z_{in} and Z_0 (377 Ω) are the impedance input of the absorber and free space, respectively; c represents the velocity of light; the microwave frequency (f) ranges from 2 to 18 GHz; and the thickness (d) of the absorber can change from 1 to 5 mm as required. According to the electromagnetic energy conversion principle,[39] the complex permittivity can be separated into its real part (ε') and imaginary part (ε''), representing the storage and dissipation capability of electrical energy, respectively. Figure 5a compares the value of ε' of Fe/N-C–RGO with those of the hollow Fe_3O_4 template and Fe/PPY–GO intermediate. The value of ε' shows the opposite tendency of that of frequency in the whole range of each sample, commonly described as the frequency dispersion effect; this phenomenon is advantageous for EMW absorption. Specifically, a steady decline in ε' from 18.68 to 9.68 of Fe/N-C–RGO is shown with slight fluctuation at high frequency. By comparison, there is a slight decrease in that of hollow Fe_3O_4 from 4.96 to 3.6, while for the nanospheres covered with PPy, the ε' value of Fe/PPY–GO remains at around 4.9 with little fluctuation. Dielectric loss consists of both conduction loss and relaxation loss according to Debye theory, which is influenced by conductivity loss and polarization loss independently.[42] The enhanced tendency of complex permittivity from hollow Fe_3O_4 to Fe/N-C–RGO is well in accordance with that of the conductivity result. The doping of nitrogen atoms further increases the conductivity of the nanocomposites, leading to increased conductivity loss. As demonstrated in Figure 5b, the ε'' value of Fe/N-C–RGO drops from the initial 9.22 to the final 0.63, compared with a slight increase from 0.46 to 1.29 of that of Fe/PPY–GO and a little oscillation at 0.15 in that of hollow Fe_3O_4. The minor fluctuation of ε'' at the high-frequency range is attributed to the shift of current lag[50] between interfaces, which is common in relative studies. Conductivity loss is caused by intrinsic and hopping conduction, which is common among carbon-based materials. It is worth noticing that some special peaks can be observed in the curves, which derive from the polarization relaxation behaviors. Polarization loss is usually classified into electronic polarization, ionic polarization, dipole orientation polarization, and interfacial polarization. In this case, introduction of both Fe and N atoms in the carbon frameworks leads to the emergence of multiple defects in the carbon-based shell, which can be regarded as polarized centers under the altering electromagnetic field, accelerating the dissipation of electromagnetic energy by orientation polarization loss. Furthermore, different interfaces among hollow cores, nanospheres, and nanosheets can induce abundant movement of the space charges, which play a dominant role in promoting the interfacial polarization effect. Herein, the Debye relaxation equation[44] is built up to demonstrate the polarization mechanism and clarify the relaxation process, which can be written as

$$\varepsilon' = \frac{\varepsilon_s - \varepsilon_\infty}{1 + \omega^2\tau^2} + \varepsilon_\infty \tag{5}$$

$$\varepsilon'' = \frac{\varepsilon_s - \varepsilon_\infty}{1 + \omega^2\tau^2}\omega\tau \tag{6}$$

$$\left(\varepsilon' - \frac{\varepsilon_s + \varepsilon_\infty}{2}\right)^2 + \varepsilon''^2 = \left(\frac{\varepsilon_s - \varepsilon_\infty}{2}\right)^2 \tag{7}$$

Here, ω, τ, ε_s, and ε_∞ are angular frequency, relaxation time, static permittivity, and relative permittivity at the high-frequency limit, respectively. Each semicircle (named as the Cole–Cole semicircle) in the plot indicates a Debye relaxation process. As can be shown in Figure S8, three semicircles were discovered in Fe/N-C–RGO; each of them represents a relaxation process. This result provides important evidence for explaining the mechanism of dielectric loss in this study when compared to no semicircle being found in Fe/PPY–GO. Normally, since it is essential in generating stronger absorption efforts toward microwave rather than reflection before permeating into the absorber, a suitable value of ε_r in the whole frequency range has a significant impact to meet the requirement. A small value of ε_r hardly contributes to microwave absorption, whereas an excessive value implies that the reflection mechanism would be predominant, leading to secondary microwave pollution. Based on previous experiments, a suitable value of ε_r is from 10 to 30. In this case, the concept of effective permittivity theory was introduced:[51]

$$\varepsilon_{eff} = \varepsilon_1\frac{(\varepsilon_2 + 2\varepsilon_1) + 2P(\varepsilon_2 - \varepsilon_1)}{(\varepsilon_2 + 2\varepsilon_1) - P(\varepsilon_2 - \varepsilon_1)} \tag{8}$$

where ε_1 represents the permittivity of the solid, ε_2 is the permittivity of the void, and P is the volume fraction of the air. According to the Maxwell–Garnett (MG) theory, which is a mechanism to identify the effective permittivity, the induction of a hollow core decreases the value of ε_{eff}, leading to the effective value of permittivity locating under this range, which has advantageous impact on microwave absorption. Dielectric loss tangent ($\tan\delta_\varepsilon$), an index calculated from the ratio of ε'' to ε', is used to illustrate the dielectric loss abilities of microwave

DOI: 10.1021/acsanm.9b02192
ACS Appl. Nano Mater. 2019, 2, 8063–8074

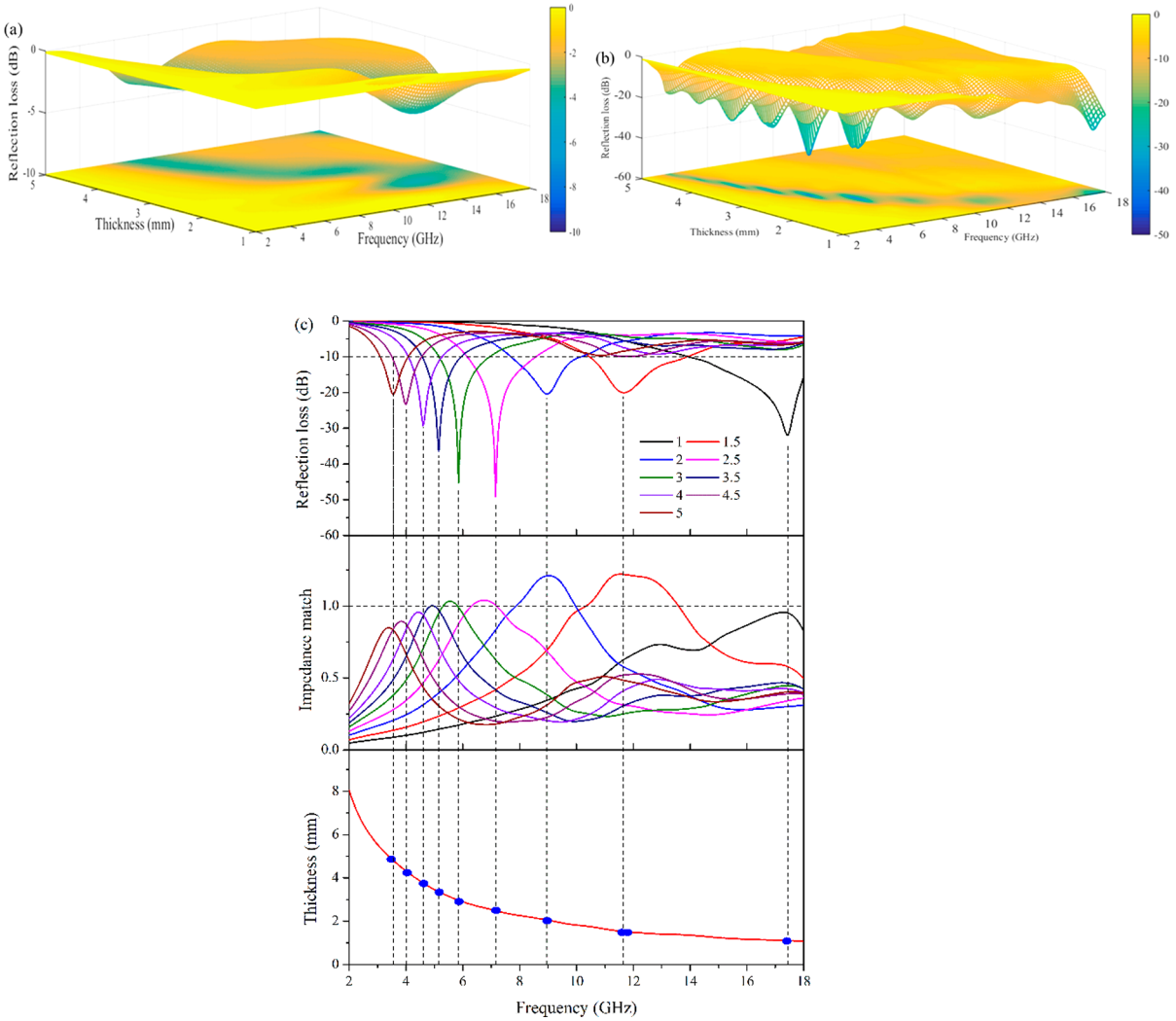

Figure 6. 3D illustration of reflection loss of Fe/PPY−GO (a), Fe/N-C−GO (b), and corresponding thickness and impedance match of Fe/N-C−RGO (c).

absorption materials (Figure S9a). Low tan δ_ε values of hollow Fe_3O_4 are ascribed to its small ε'' value in the whole specific frequency range. The higher tan δ_ε value of Fe/N-C−RGO, especially before 14 GHz, confirms that Fe/N-C−RGO has more powerful dielectric loss capacities than the relevant precursor and intermediate at lower frequency.

Magnetic loss[52] is usually believed to originate from different resonance behaviors, magnetic hysteresis, and eddy current effect. However, the frequency ranges from 2 to 18 GHz in this case. Thus, the magnetic loss is only attenuated by the mechanisms of natural resonance, exchange resonance, and eddy current effect, because magnetic hysteresis originates from irreversible magnetization at higher frequency regions, and domain wall resonance commonly occurs below 2 GHz. Figure 5c,d illustrates the variation of the real part (μ') and the imaginary part (μ'') of the complex permeability in the range of 2−18 GHz. The μ' value of Fe/PPY−GO remains almost constant with slight fluctuations in the whole frequency range, caused by the reduction of Fe_3O_4 while growing the PPy shells, exhibiting negligible magnetic loss. For hollow Fe_3O_4, small peaks occur because of its intrinsic ferromagnetic properties, while similar but stronger peaks are inherited by Fe/N-C−RGO after the decomposition of PPy into Fe/N-codoped carbonaceous shells. The Fe^{3+} ions also serve as ferromagnetic active sites that offer magnetic-loss behaviors, even though the amount of Fe^{3+} ions is not large. There is a rapid increase in the value of μ'' from 0.09 to 1.19 of Fe/N-C−RGO. Two distinguished peaks, which can be recognized at nearly 13.8 GHz, correspond to the natural resonance and exchange resonance behaviors, respectively.[53] Similar peaks also occurred in the μ''−frequency curves of hollow Fe_3O_4, which can be ascribed to the same mechanism. The introduction of nonmagnetic compositions contributes to the decrease of ferromagnetism, leading to the anticipation of those peaks. In addition, in order to evaluate the eddy current effect toward magnetic loss behaviors, the characterized equation is introduced as follows:[54]

$$\mu'' \mu'^{-2} f^{-1} = \frac{2}{3}\pi\mu_0 d^2\sigma \tag{9}$$

where μ_0 represents the vacuum permeability, σ represents the electric conductivity, and d represents the thickness of the sample, which are constant for an independent sample. Therefore, if the value of left part of the equation remains constant as C_0 under the variation of the frequency, the eddy current effect is the only factor contributing to magnetic loss. In this case (Figure S10), the value fluctuates in the whole frequency range, indicating a major contribution of multiple resonance behaviors to the magnetic loss, along with a weak

DOI: 10.1021/acsanm.9b02192
ACS Appl. Nano Mater. 2019, 2, 8063−8074

contribution of eddy current. Representing the dissipation ability of magnetic energy, the magnetic loss tangent ($\tan \delta_\mu$) is calculated similarly to $\tan \delta_\varepsilon$, shown in Figure S9b. The values of $\tan \delta_\mu$ correspond with those of μ'', demonstrating that the dominant mechanisms are related to what has been mentioned above. These correlated loss effects significantly broaden the effective bandwidth as well as improve the intensity of the reflection loss, especially at high frequency when the thickness of the sample is thin.

Reflection loss (RL) is an index used to systemically evaluate the microwave absorption properties under the guideline of transition/reflection theory. In addition, the effective absorption bandwidth (EAB) of RL value, representing the frequency range with the value of RL under −10 dB, is also required, since EAB represents the bandwidth that more than 90% of the microwave is attenuated, which has essential influence on practical applications. Calculated using eqs 3 and 4 for a specific frequency range with specific thickness, Figures 6 and S11 show the 2D and 3D figures of reflection loss depending on frequency and thickness of Fe/N-C−RGO, Fe/PPY−GO intermediate, and hollow Fe_3O_4.precursor. Naturally, the RL peaks are pushed toward frequency contrasting with the thickness trend, which is in correspondence with other articles.[39] However, the absorption properties are different. For hollow Fe_3O_4 (Figure 6a), the maximum RL value is −10.14 dB with a thickness of 5 mm, due to the mismatch of moderate magnetic loss and weak dielectric loss. In addition, the EAB is too narrow to be distinguished by different thickness. The weak reflection loss intensity cannot meet the requirement of next-generation microwave absorber. Through introducing heterogeneous compositions, the characteristic peaks can be separated, which means that the microwave can be absorbed to a certain extent with the same thickness. However, the reflection loss behaviors of Fe/PPY−GO are even worse due to the hindrance in magnetic loss and lack of adequate conductivity loss. By comparison, Fe/N-C−RGO (Figures 6b,c) reaches the most outstanding RL peak value of −49.08 dB at 7.15 GHz when the thickness is 2.5 mm. Additionally, the effective absorption bandwidth covers from 6.1 to 8.65 GHz at this thickness. Furthermore, ultrawide effective absorption bandwidth can be achieved while the thickness is only 1 mm from 13.75 to 18 GHz. Moreover, the demand of operation for various frequency bands from 3.1 to 18 GHz can be feasibly satisfied by tuning the thickness of the sample. The growth of Fe/N-carbon nanospheres on the surface of N-graphene also has significant contribution toward microwave absorption when compared to the Fe/N-codoped hollow carbonaceous nanospheres (Figure S12). It can be seen that the minimum value of reflection loss (RL) only reaches −25 dB with narrow effective absorption bandwidth (EAB) in Fe/N-codoped hollow carbonaceous nanospheres, resulting from the weak dielectric loss behaviors. Through combination with reduced graphene oxide, the dielectric loss behavior was strengthened in a broad frequency range, contributing to the increasing value of RL, along with the expansion of EAB. In addition, in order to find out the best microwave absorption performance with different polymerization time (Fe content), comparable experiments were performed, and the RL values are shown in Figure S13. The reflection loss behavior did not change much when the polymerization time was 5 min, perhaps caused by the reaction just reacted. With continuing the reaction, the EAB began to broaden, which was obvious after 20 min. However, overlong reaction time (120 min) incurred the exhaustion of Fe atoms, which re-dissolved in the solution finally, synthesizing N-doped carbonaceous nanospheres anchored on graphene oxide. Magnetic loss was insufficient, attributed to scarcity of Fe atoms, leading to a worse microwave absorption performance when compared with the reaction time at 60 min.

Furthermore, according to quarter-wavelength theory,[35] when the matching thickness (t_m) of the nanomaterials is linearly dependent on an odd multiple of the quarter wavelength (λ_m),

$$t_m = \frac{n\lambda_m}{4} = \frac{nc}{4f_m\sqrt{|\varepsilon_r||\mu_r|}} \qquad n = 1, 3, 5, \ldots \tag{10}$$

$$Z = \frac{Z_{in}}{Z_0} \tag{11}$$

an optimal value of the reflection loss could be obtained. As can be shown in Figure 6c, the peaks of RL with various thickness drop onto the characteristic line of t_m. This circumstance corresponds to the impedance match (Z) mechanism, while the value of Z is around 1 in a unique frequency. An excellent microwave absorber demands both strong microwave attenuation abilities and enough impedance matching characteristics to enable absorption. For Fe/N-C−RGO, the peaks of each plot also correspond well to the value of Z, which means that the microwaves can enter inside the absorbers rather than being reflected on the surface, preventing secondary pollution of unwanted microwave radiation. In this situation, it can be indicated that the absorption loss properties are overwhelmingly dependent on this mechanism. Moreover, the attenuation constant α is employed by the following equation to estimate the attenuation ability of the entering microwave:[55]

$$\alpha = \frac{\sqrt{2}\pi f}{c}\left((\mu''\varepsilon'' - \mu'\varepsilon') + \sqrt{(\mu''\varepsilon'' - \mu'\varepsilon')^2 + (\mu'\varepsilon'' + \mu''\varepsilon')^2}\right)^{1/2} \tag{12}$$

As shown in Figure S14, while the value of α increases with frequency, the value for Fe/N-C−RGO is stronger than that for hollow Fe_3O_4 and Fe/PPY−GO, especially in the high-frequency region, indicating the enhancement of attenuation ability for incident EMW after undergoing polymerization and calcination processes. The whole dissipation mechanism is illustrated in Figure 7.

The enhanced microwave absorption performance can be explained through several aspects: (1) The optimized designed structure between 0-dimensional nanospheres and 2-dimensional nanosheets constructs a conductive network, while the

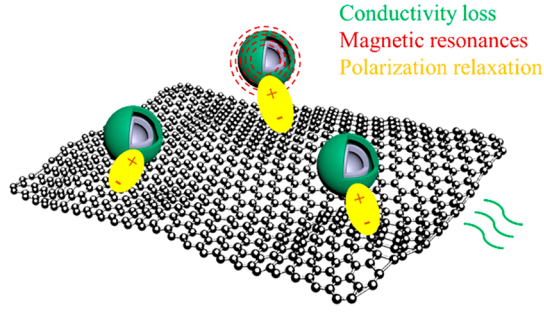

Figure 7. Microwave loss mechanisms of Fe/N-C−RGO.

DOI: 10.1021/acsanm.9b02192
ACS Appl. Nano Mater. 2019, 2, 8063−8074

Table 1. Comparison of the Microwave Absorption Properties of Ferromagnetic-Carbon-Based Samples

sample	mass ratio of absorber (%)	optimal RL value (dB)	f at optimal RL (GHz)	d (mm)	bandwidth over −10 dB (GHz)	ref
Cu@Ni-RGO		−41.2	8.8	2.5	3.8−18	58
RGO/Fe_3O_4/ZnO	33.3	−57.0	13.5	2	5.9−16.7	59
$NiFe_2O_4$/G	15	−40.9	8.32	3.5	4−18	60
Fe_3O_4/CNT	30	−43	15.2	1.5	9.7−18	61
RGO/$MnFe_2O_4$	5	−29	9.2	3	8−12.88	62
Fe_3O_4/PPY	50	−41.9	13.3	2	3.9−18	63
Ni/RGO	30	−49.0	5.3	4	3.2−18	64
G/Fe_3O_4@Fe	20	−35.2	17.8	2	4−18	36
$CoFe_2O_4$/RGO	20	−46.8	11.6	1.6	4.9−18	65
FeCo/C/$CoFe_2O_4$	50	−38.1	13.4	7.5	11.3−18	66
Fe_3O_4/CNT	10	−24.8	9	3.2	8.2−12.4	67
$ZrN_{0.4}B_{0.6}$/SiC	80	−50.8	7.7	3.05	6.5−9.3	68
Fe−Fe_3O_4@C	30	−39.1	15.9	2	5.2−18	69
Fe_3O_4/GCs	30	−32	8.76	3.5	5.4−17	53
Fe/N-C−RGO	**5**	**−49.08**	**7.15**	**2.5**	**3.1−18**	**this work**

dopant of N atoms increases the electric conductivity, leading to better conductivity loss. (2) This nanostructure features a large number of interfaces, which can be seen as capacitor-like structures,[56,57] improving relaxation loss deriving from interfacial polarization and dipole polarization. These performances can be demonstrated by comparing with the poor microwave absorption performance of hollow Fe_3O_4 and Fe/PPY−GO intermediate, which offer fewer interfaces. (3) The hollow cores decrease the effective value of permittivity in a suitable range, while the Fe atoms serve as ferromagnetic active sites. The synergistic effect between them balances the impedance match between dielectric loss and magnetic loss, optimizing the microwave absorption response rather than reflection response at the moment when the absorber is exposed in an electromagnetic field. Furthermore, the hollow cores decrease the density, which meets the requirement for lightweight absorbers. (4) Additionally, this unique structure prolongs the pathway of the microwaves that propagate inside, leading to a transformation from microwave energy into heat and finally exhausted.[47] Thus, lightweight, low thickness, wide bandwidth, and strong absorption intensity properties were gathered in this nanocomposite, which meets the requirement toward the next-generation microwave absorbers. The comparison with other nanocomposites possessing similar structure is shown in Table 1.

4. CONCLUSION

Generally, an easily operated and novel method was adopted to synthesize Fe/N-codoped hollow carbonaceous nanospheres anchored on reduced graphene oxide nanosheets by sacrificing the precursor with controllable oxidized polymerization and high-temperature pyrolysis process. Superior microwave absorption properties can be acquired after making great efforts to combine the effects of dielectric loss, magnetic loss, and energy conversion from specific nanostructures. At first, the ferromagnetic properties of residual Fe have an essential effect on magnetic loss, which will influence microwave absorption ability. Meanwhile, interfacial polarization is considerably improved from a core-in-hollow/shell structure together with 0D−2D nanocomposites. In addition, dielectric loss is also strengthened by dipole polarization because the doping of Fe/N atoms offers more active sites for electric carriers (space charges) to transport in specified and directional pathways. After penetrating different layers, the electromagnetic wave energy is transformed into heat energy due to the synergistic effect of conductivity loss, interfacial polarization, dipole polarization, and multiple resonance behaviors. Overall, the controllable synthesis of Fe/N-C−RGO provides a promising electromagnetic wave absorber with strong reflection loss, thin thickness, wide effective response bandwidth, and ultralight weight, which has great potential in next-generation cutting-edge advanced nanocomposites.

■ ASSOCIATED CONTENT

Supporting Information

The Supporting Information is available free of charge at https://pubs.acs.org/doi/10.1021/acsanm.9b02192.

Method of production of GO sheets, Raman spectra and SEM of hollow Fe_3O_4 on RGO, AFM image of RGO, M-H plot of Fe_3O_4 nanospheres, XPS and FT-IR spectra of Fe/N-C−RGO, N_2 adsorption−desorption isotherm of Fe/N-C−RGO, HR-TEM of nanosphere edge, Cole−Cole plots of Fe/N-C−RGO and Fe/PPY−GO, dielectric and magnetic loss factors, eddy current effect, reflection loss of hollow Fe_3O_4, Fe/PPY−GO, and Fe/N-co-doped carbon nanospheres, reflection loss with different polymerization times, attenuation constant, and iron content with different polymerization times (PDF)

■ AUTHOR INFORMATION

Corresponding Author

*E-mail: lih@sjtu.edu.cn. Tel: +86 021 34202549.

ORCID

Yujie Chen: 0000-0003-2513-7559

Hua Li: 0000-0003-2852-4722

Qinglei Liu: 0000-0003-0677-3613

Notes

The authors declare no competing financial interest.

■ ACKNOWLEDGMENTS

H.L. is thankful for the support from the National Natural Science Foundation of China (No. 51373096, 81772432, U1733130), Basic Research Field of Shanghai Science and Technology Innovation Program (No.16JC1401500), Science and Technology Innovation Special Zone Program (No. 18-163-13-ZT-008-003-06) and Cross Research Fund of Bio-

DOI: 10.1021/acsanm.9b02192
ACS Appl. Nano Mater. 2019, 2, 8063−8074

medical Engineering of Shanghai Jiao Tong University (YG2016MS70).

REFERENCES

(1) Cao, M. S.; Wang, X. X.; Cao, W. Q.; Yuan, J. Ultrathin Graphene: Electrical Properties and Highly Efficient Electromagnetic Interference Shielding. *J. Mater. Chem. C* **2015**, *3* (26), 6589−6599.
(2) Chung, D. Electromagnetic Interference Shielding Effectiveness of Carbon Materials. *Carbon* **2001**, *39* (2), 279−285.
(3) Geetha, S.; Satheesh Kumar, K.; Rao, C. R.; Vijayan, M.; Trivedi, D. Emi Shielding: Methods and Materials—a Review. *J. Appl. Polym. Sci.* **2009**, *112* (4), 2073−2086.
(4) Qin, F.; Brosseau, C. A Review and Analysis of Microwave Absorption in Polymer Composites Filled with Carbonaceous Particles. *J. Appl. Phys.* **2012**, *111* (6), 061301.
(5) Sun, X.; Sheng, L.; Yang, J.; An, K.; Yu, L.; Zhao, X. Three-Dimensional (3d) Reduced Graphene Oxide (Rgo)/Zinc Oxide (Zno)/Barium Ferrite Nanocomposites for Electromagnetic Absorption. *J. Mater. Sci.: Mater. Electron.* **2017**, *28* (17), 12900−12908.
(6) Li, Y.; Fang, X.; Cao, M. Thermal Frequency Shift and Tunable Microwave Absorption in Bifeo3 Family. *Sci. Rep.* **2016**, *6*, 24837.
(7) Liang, C.; Liu, C.; Wang, H.; Wu, L.; Jiang, Z.; Xu, Y.; Shen, B.; Wang, Z. Sic-Fe3o4dielectric-Magnetic Hybrid Nanowires: Controllable Fabrication, Characterization and Electromagnetic Wave Absorption. *J. Mater. Chem. A* **2014**, *2* (39), 16397−16402.
(8) He, J.-Z.; Wang, X.-X.; Zhang, Y.-L.; Cao, M.-S. Small Magnetic Nanoparticles Decorating Reduced Graphene Oxides to Tune the Electromagnetic Attenuation Capacity. *J. Mater. Chem. C* **2016**, *4* (29), 7130−7140.
(9) Kaur, P.; Chawla, S.; Narang, S. B.; Pubby, K. Structural, Magnetic and Microwave Absorption Behavior of Co-Zr Substituted Strontium Hexaferrites Prepared Using Tartaric Acid Fuel for Electromagnetic Interference Suppression. *J. Magn. Magn. Mater.* **2017**, *422*, 304−314.
(10) He, C.; Qiu, S.; Wang, X.; Liu, J.; Luan, L.; Liu, W.; Itoh, M.; Machida, K.-i. Facile Synthesis of Hollow Porous Cobalt Spheres and Their Enhanced Electromagnetic Properties. *J. Mater. Chem.* **2012**, *22* (41), 22160.
(11) Ma, F.; Qin, Y.; Li, Y.-Z. Enhanced Microwave Performance of Cobalt Nanoflakes with Strong Shape Anisotropy. *Appl. Phys. Lett.* **2010**, *96* (20), 202507.
(12) Wang, C.; Han, X.; Zhang, X.; Hu, S.; Zhang, T.; Wang, J.; Du, Y.; Wang, X.; Xu, P. Controlled Synthesis and Morphology-Dependent Electromagnetic Properties of Hierarchical Cobalt Assemblies. *J. Phys. Chem. C* **2010**, *114* (35), 14826−14830.
(13) Tong, G.; Yuan, J.; Wu, W.; Hu, Q.; Qian, H.; Li, L.; Shen, J. Flower-Like Co Superstructures: Morphology and Phase Evolution Mechanism and Novel Microwave Electromagnetic Characteristics. *CrystEngComm* **2012**, *14* (6), 2071.
(14) Kang, J.; Kim, D.; Kim, Y.; Choi, J.-B.; Hong, B. H.; Kim, S. W. High-Performance near-Field Electromagnetic Wave Attenuation in Ultra-Thin and Transparent Graphene Films. *2D Mater.* **2017**, *4* (2), 025003.
(15) Zhao, T.; Hou, C.; Zhang, H.; Zhu, R.; She, S.; Wang, J.; Li, T.; Liu, Z.; Wei, B. Electromagnetic Wave Absorbing Properties of Amorphous Carbon Nanotubes. *Sci. Rep.* **2015**, *4*, 5619.
(16) Song, W. L.; Cao, M. S.; Lu, M. M.; Yang, J.; Ju, H. F.; Hou, Z. L.; Liu, J.; Yuan, J.; Fan, L. Z. Alignment of Graphene Sheets in Wax Composites for Electromagnetic Interference Shielding Improvement. *Nanotechnology* **2013**, *24* (11), 115708.
(17) Wan, Y.-J.; Zhu, P.-L.; Yu, S.-H.; Sun, R.; Wong, C.-P.; Liao, W.-H. Graphene Paper for Exceptional Emi Shielding Performance Using Large-Sized Graphene Oxide Sheets and Doping Strategy. *Carbon* **2017**, *122*, 74−81.
(18) Zhao, H.; Cheng, Y.; Liu, W.; Yang, L.; Zhang, B.; Wang, L. P.; Ji, G.; Xu, Z. J. Biomass-Derived Porous Carbon-Based Nanostructures for Microwave Absorption. *Nano-Micro Lett.* **2019**, *11*, 24.
(19) Kar, G. P.; Biswas, S.; Bose, S. Tuning the Microwave Absorption through Engineered Nanostructures in Co-Continuous Polymer Blends. *Mater. Res. Express* **2016**, *3* (6), 064002.
(20) Wu, Y.; Wang, Z.; Liu, X.; Shen, X.; Zheng, Q.; Xue, Q.; Kim, J.-K. Ultralight Graphene Foam/Conductive Polymer Composites for Exceptional Electromagnetic Interference Shielding. *ACS Appl. Mater. Interfaces* **2017**, *9* (10), 9059−9069.
(21) Hsiao, S.-T.; Ma, C.-C. M.; Liao, W.-H.; Wang, Y.-S.; Li, S.-M.; Huang, Y.-C.; Yang, R.-B.; Liang, W.-F. Lightweight and Flexible Reduced Graphene Oxide/Water-Borne Polyurethane Composites with High Electrical Conductivity and Excellent Electromagnetic Interference Shielding Performance. *ACS Appl. Mater. Interfaces* **2014**, *6* (13), 10667−10678.
(22) Wang, G.-S.; Wu, Y.-Y.; Zhang, X.-J.; Li, Y.; Guo, L.; Cao, M.-S. Controllable Synthesis of Uniform Zno Nanorods and Their Enhanced Dielectric and Absorption Properties. *J. Mater. Chem. A* **2014**, *2* (23), 8644−8651.
(23) Xia, T.; Zhang, C.; Oyler, N. A.; Chen, X. Hydrogenated Tio2 Nanocrystals: A Novel Microwave Absorbing Material. *Adv. Mater.* **2013**, *25* (47), 6905−6910.
(24) Xia, T.; Cao, Y.; Oyler, N. A.; Murowchick, J.; Liu, L.; Chen, X. Strong Microwave Absorption of Hydrogenated Wide Bandgap Semiconductor Nanoparticles. *ACS Appl. Mater. Interfaces* **2015**, *7* (19), 10407−10413.
(25) Zhang, M.; Wang, X. X.; Cao, W. Q.; Yuan, J.; Cao, M. S. Electromagnetic Functions of Patterned 2d Materials for Micro-Nano Devices Covering Ghz, Thz, and Optical Frequency. *Adv. Opt. Mater.* **2019**, *7* (19), 1900689.
(26) Cao, M. S.; Wang, X. X.; Zhang, M.; Shu, J. C.; Cao, W. Q.; Yang, H. J.; Fang, X. Y.; Yuan, J. Electromagnetic Response and Energy Conversion for Functions and Devices in Low-Dimensional Materials. *Adv. Funct. Mater.* **2019**, *29* (25), 1807398.
(27) Putri, L. K.; Ong, W.-J.; Chang, W. S.; Chai, S.-P. Heteroatom Doped Graphene in Photocatalysis: A Review. *Appl. Surf. Sci.* **2015**, *358*, 2−14.
(28) Wang, H.; Maiyalagan, T.; Wang, X. Review on Recent Progress in Nitrogen-Doped Graphene: Synthesis, Characterization, and Its Potential Applications. *ACS Catal.* **2012**, *2* (5), 781−794.
(29) Sheng, Z.-H.; Shao, L.; Chen, J.-J.; Bao, W.-J.; Wang, F.-B.; Xia, X.-H. Catalyst-Free Synthesis of Nitrogen-Doped Graphene Via Thermal Annealing Graphite Oxide with Melamine and Its Excellent Electrocatalysis. *ACS Nano* **2011**, *5* (6), 4350−4358.
(30) Wu, T.; Liu, Y.; Zeng, X.; Cui, T.; Zhao, Y.; Li, Y.; Tong, G. Facile Hydrothermal Synthesis of Fe3o4/C Core-Shell Nanorings for Efficient Low-Frequency Microwave Absorption. *ACS Appl. Mater. Interfaces* **2016**, *8* (11), 7370−80.
(31) Che, R. C.; Peng, L. M.; Duan, X. F.; Chen, Q.; Liang, X. Microwave Absorption Enhancement and Complex Permittivity and Permeability of Fe Encapsulated within Carbon Nanotubes. *Adv. Mater.* **2004**, *16* (5), 401−405.
(32) Du, Y.; Liu, W.; Qiang, R.; Wang, Y.; Han, X.; Ma, J.; Xu, P. Shell Thickness-Dependent Microwave Absorption of Core-Shell Fe3o4@C Composites. *ACS Appl. Mater. Interfaces* **2014**, *6* (15), 12997−3006.
(33) Zhao, H.; Cheng, Y.; Lv, H.; Ji, G.; Du, Y. A Novel Hierarchically Porous Magnetic Carbon Derived from Biomass for Strong Lightweight Microwave Absorption. *Carbon* **2019**, *142*, 245−253.
(34) Zhou, N.; An, Q.; Xiao, Z.; Zhai, S.; Shi, Z. Rational Design of Superior Microwave Shielding Composites Employing Synergy of Encapsulating Character of Alginate Hydrogels and Task-Specific Components (Ni Nps, Fe3o4/Cnts). *ACS Sustainable Chem. Eng.* **2017**, *5* (6), 5394−5407.
(35) Ding, D.; Wang, Y.; Li, X.; Qiang, R.; Xu, P.; Chu, W.; Han, X.; Du, Y. Rational Design of Core-Shell Co@ C Microspheres for High-Performance Microwave Absorption. *Carbon* **2017**, *111*, 722−732.
(36) Ren, Y.-L.; Wu, H.-Y.; Lu, M.-M.; Chen, Y.-J.; Zhu, C.-L.; Gao, P.; Cao, M.-S.; Li, C.-Y.; Ouyang, Q.-Y. Quaternary Nanocomposites Consisting of Graphene, Fe3o4@ Fe Core@ Shell, and Zno Nanoparticles: Synthesis and Excellent Electromagnetic Absorption Properties. *ACS Appl. Mater. Interfaces* **2012**, *4* (12), 6436−6442.
(37) Chen, Y.-J.; Xiao, G.; Wang, T.-S.; Ouyang, Q.-Y.; Qi, L.-H.; Ma, Y.; Gao, P.; Zhu, C.-L.; Cao, M.-S.; Jin, H.-B. Porous Fe3o4/Carbon

DOI: 10.1021/acsanm.9b02192
ACS Appl. Nano Mater. 2019, 2, 8063−8074

Core/Shell Nanorods: Synthesis and Electromagnetic Properties. *J. Phys. Chem. C* **2011**, *115* (28), 13603−13608.
(38) Li, D.; Liao, H.; Kikuchi, H.; Liu, T. Microporous Co@C Nanoparticles Prepared by Dealloying Coal@C Precursors: Achieving Strong Wideband Microwave Absorption Via Controlling Carbon Shell Thickness. *ACS Appl. Mater. Interfaces* **2017**, *9* (51), 44704−44714.
(39) Wang, K.; Chen, Y.; Tian, R.; Li, H.; Zhou, Y.; Duan, H.; Liu, H. Porous Co-C Core-Shell Nanocomposites Derived from Co-Mof-74 with Enhanced Electromagnetic Wave Absorption Performance. *ACS Appl. Mater. Interfaces* **2018**, *10* (13), 11333−11342.
(40) Wu, H.; Wu, G.; Ren, Y.; Li, X.; Wang, L. Multishelled Metal Oxide Hollow Spheres: Easy Synthesis and Formation Mechanism. *Chem. - Eur. J.* **2016**, *22* (26), 8864−71.
(41) Cheng, Y.; Cao, J.; Li, Y.; Li, Z.; Zhao, H.; Ji, G.; Du, Y. The Outside-in Approach to Construct Fe3o4 Nanocrystals/Mesoporous Carbon Hollow Spheres Core-Shell Hybrids toward Microwave Absorption. *ACS Sustainable Chem. Eng.* **2018**, *6* (1), 1427−1435.
(42) Quan, B.; Shi, W.; Ong, S. J. H.; Lu, X.; Wang, P. L.; Ji, G.; Guo, Y.; Zheng, L.; Xu, Z. J. Defect Engineering in Two Common Types of Dielectric Materials for Electromagnetic Absorption Applications. *Adv. Funct. Mater.* **2019**, *29* (28), 1901236.
(43) Huang, Z.; Pan, H.; Yang, W.; Zhou, H.; Gao, N.; Fu, C.; Li, S.; Li, H.; Kuang, Y. In Situ Self-Template Synthesis of Fe-N-Doped Double-Shelled Hollow Carbon Microspheres for Oxygen Reduction Reaction. *ACS Nano* **2018**, *12* (1), 208−216.
(44) Tian, C.; Du, Y.; Xu, P.; Qiang, R.; Wang, Y.; Ding, D.; Xue, J.; Ma, J.; Zhao, H.; Han, X. Constructing Uniform Core-Shell Ppy@Pani Composites with Tunable Shell Thickness toward Enhancement in Microwave Absorption. *ACS Appl. Mater. Interfaces* **2015**, *7* (36), 20090−9.
(45) Xu, P.; Han, X.; Wang, C.; Zhou, D.; Lv, Z.; Wen, A.; Wang, X.; Zhang, B. Synthesis of Electromagnetic Functionalized Nickel/Polypyrrole Core/Shell Composites. *J. Phys. Chem. B* **2008**, *112* (34), 10443−10448.
(46) Liu, W.; Liu, L.; Yang, Z.; Xu, J.; Hou, Y.; Ji, G. A Versatile Route toward the Electromagnetic Functionalization of Metal-Organic Framework-Derived Three-Dimensional Nanoporous Carbon Composites. *ACS Appl. Mater. Interfaces* **2018**, *10* (10), 8965−8975.
(47) Cao, M.; Wang, X.; Cao, W.; Fang, X.; Wen, B.; Yuan, J. Thermally Driven Transport and Relaxation Switching Self-Powered Electromagnetic Energy Conversion. *Small* **2018**, *14*, No. e1800987.
(48) Zhou, Y.; Tian, R.; Duan, H.; Wang, K.; Guo, Y.; Li, H.; Liu, H. Cose/Co Nanoparticles Wrapped by in Situ Grown N-Doped Graphitic Carbon Nanosheets as Anode Material for Advanced Lithium Ion Batteries. *J. Power Sources* **2018**, *399*, 223−230.
(49) Wen, B.; Cao, M.; Lu, M.; Cao, W.; Shi, H.; Liu, J.; Wang, X.; Jin, H.; Fang, X.; Wang, W.; Yuan, J. Reduced Graphene Oxides: Light-Weight and High-Efficiency Electromagnetic Interference Shielding at Elevated Temperatures. *Adv. Mater.* **2014**, *26* (21), 3484−9.
(50) Liu, X. G.; Geng, D. Y.; Meng, H.; Shang, P. J.; Zhang, Z. D. Microwave-Absorption Properties of Zno-Coated Iron Nanocapsules. *Appl. Phys. Lett.* **2008**, *92* (17), 173117.
(51) Wang, L.; Zhou, P.; Guo, Y.; Zhang, J.; Qiu, X.; Guan, Y.; Yu, M.; Zhu, H.; Zhang, Q. The Effect of Zncl2 Activation on Microwave Absorbing Performance in Walnut Shell-Derived Nano-Porous Carbon. *RSC Adv.* **2019**, *9* (17), 9718−9728.
(52) Van der Zaag, P. New Views on the Dissipation in Soft Magnetic Ferrites. *J. Magn. Magn. Mater.* **1999**, *196*, 315−319.
(53) Jian, X.; Wu, B.; Wei, Y.; Dou, S. X.; Wang, X.; He, W.; Mahmood, N. Facile Synthesis of Fe3o4/Gcs Composites and Their Enhanced Microwave Absorption Properties. *ACS Appl. Mater. Interfaces* **2016**, *8* (9), 6101−9.
(54) Zhang, X.; Ji, G.; Liu, W.; Zhang, X.; Gao, Q.; Li, Y.; Du, Y. A Novel Co/Tio2 Nanocomposite Derived from a Metal-Organic Framework: Synthesis and Efficient Microwave Absorption. *J. Mater. Chem. C* **2016**, *4* (9), 1860−1870.
(55) Cheng, Y.; Zhao, Y.; Zhao, H.; Lv, H.; Qi, X.; Cao, J.; Ji, G.; Du, Y. Engineering Morphology Configurations of Hierarchical Flower-Like Mose2 Spheres Enable Excellent Low-Frequency and Selective Microwave Response Properties. *Chem. Eng. J.* **2019**, *372*, 390−398.
(56) Ma, J.; Wang, X.; Cao, W.; Han, C.; Yang, H.; Yuan, J.; Cao, M. A Facile Fabrication and Highly Tunable Microwave Absorption of 3d Flower-Like Co3o4-Rgo Hybrid-Architectures. *Chem. Eng. J.* **2018**, *339*, 487−498.
(57) Cao, W.-Q.; Wang, X.-X.; Yuan, J.; Wang, W.-Z.; Cao, M.-S. Temperature Dependent Microwave Absorption of Ultrathin Graphene Composites. *J. Mater. Chem. C* **2015**, *3* (38), 10017−10022.
(58) Zhao, B.; Liang, L.; Deng, J.; Bai, Z.; Liu, J.; Guo, X.; Gao, K.; Guo, W.; Zhang, R. 1d Cu@Ni Nanorods Anchored on 2d Reduced Graphene Oxide with Interfacial Engineering to Enhance Microwave Absorption Properties. *CrystEngComm* **2017**, *19* (44), 6579−6587.
(59) Zhang, N.; Huang, Y.; Wang, M. 3d Ferromagnetic Graphene Nanocomposites with Zno Nanorods and Fe 3 O 4 Nanoparticles Co-Decorated for Efficient Electromagnetic Wave Absorption. *Composites, Part B* **2018**, *136*, 135−142.
(60) Yan, F.; Guo, D.; Zhang, S.; Li, C.; Zhu, C.; Zhang, X.; Chen, Y. An Ultra-Small Nife2o4 Hollow Particle/Graphene Hybrid: Fabrication and Electromagnetic Wave Absorption Property. *Nanoscale* **2018**, *10* (6), 2697−2703.
(61) Li, N.; Huang, G. W.; Li, Y. Q.; Xiao, H. M.; Feng, Q. P.; Hu, N.; Fu, S. Y. Enhanced Microwave Absorption Performance of Coated Carbon Nanotubes by Optimizing the Fe3o4 Nanocoating Structure. *ACS Appl. Mater. Interfaces* **2017**, *9* (3), 2973−2983.
(62) Zhang, X. J.; Wang, G. S.; Cao, W. Q.; Wei, Y. Z.; Liang, J. F.; Guo, L.; Cao, M. S. Enhanced Microwave Absorption Property of Reduced Graphene Oxide (Rgo)-Mnfe2o4 Nanocomposites and Polyvinylidene Fluoride. *ACS Appl. Mater. Interfaces* **2014**, *6* (10), 7471−8.
(63) Wu, Z.; Tan, D.; Tian, K.; Hu, W.; Wang, J.; Su, M.; Li, L. Facile Preparation of Core-Shell Fe3o4@Polypyrrole Composites with Superior Electromagnetic Wave Absorption Properties. *J. Phys. Chem. C* **2017**, *121* (29), 15784−15792.
(64) Lai, Y.; Wang, S.; Qian, D.; Zhong, S.; Wang, Y.; Han, S.; Jiang, W. Tunable Electromagnetic Wave Absorption Properties of Nickel Microspheres Decorated Reduced Graphene Oxide. *Ceram. Int.* **2017**, *43* (15), 12904−12914.
(65) Zhang, K.; Gao, X.; Zhang, Q.; Li, T.; Chen, H.; Chen, X. Preparation and Microwave Absorption Properties of Asphalt Carbon Coated Reduced Graphene Oxide/Magnetic Cofe2o4 Hollow Particles Modified Multi-Wall Carbon Nanotube Composites. *J. Alloys Compd.* **2017**, *723*, 912−921.
(66) Feng, Y.; Li, D.; Jiang, L.; Dai, Z.; Wang, Y.; An, J.; Ren, W.; He, J.; Wang, Z.; Liu, W.; Zhang, Z. Interface Transformation for Enhanced Microwave-Absorption Properties of Core Double-Shell Nanocomposites. *J. Alloys Compd.* **2017**, *694*, 1224−1231.
(67) Lu, M. M.; Cao, M. S.; Chen, Y. H.; Cao, W. Q.; Liu, J.; Shi, H. L.; Zhang, D. Q.; Wang, W. Z.; Yuan, J. Multiscale Assembly of Grape-Like Ferroferric Oxide and Carbon Nanotubes: A Smart Absorber Prototype Varying Temperature to Tune Intensities. *ACS Appl. Mater. Interfaces* **2015**, *7* (34), 19408−15.
(68) Jian, X.; Tian, W.; Li, J.; Deng, L.; Zhou, Z.; Zhang, L.; Lu, H.; Yin, L.; Mahmood, N. High-Temperature Oxidation-Resistant Zrn0.4b0.6/Sic Nanohybrid for Enhanced Microwave Absorption. *ACS Appl. Mater. Interfaces* **2019**, *11* (17), 15869−15880.
(69) Jian, X.; Xiao, X.; Deng, L.; Tian, W.; Wang, X.; Mahmood, N.; Dou, S. Heterostructured Nanorings of Fe-Fe3o4@C Hybrid with Enhanced Microwave Absorption Performance. *ACS Appl. Mater. Interfaces* **2018**, *10* (11), 9369−9378.

DOI: 10.1021/acsanm.9b02192
ACS Appl. Nano Mater. 2019, 2, 8063−8074